

$\text{Al}_x\text{Ga}_{1-x}\text{As}$ crystals with direct 2 eV band gaps from computational alchemy

K. Y. Samuel Chang¹ and O. Anatole von Lilienfeld^{1,*}

¹*Institute of Physical Chemistry and National Center for Computational Design and Discovery of Novel Materials (MARVEL), Department of Chemistry, University of Basel, 4056 Basel, Switzerland*
(Dated: May 15, 2022)

We design $\text{Al}_x\text{Ga}_{1-x}\text{As}$ crystals with large direct band gap using computational alchemy within a genetic algorithm. Dozens of crystal polymorphs are identified for $x > \frac{2}{3}$ with direct band gaps larger than 2 eV according to HSE approximated density functional theory. Based on a single generalized gradient approximated density functional theory band structure calculation of pure GaAs we observe convergence after visiting only ~ 800 crystal candidates. The general applicability of alchemical gradients is further corroborated by ranking the uptake of H_2 in Sr and Ca-alanate crystals.

Major advancements of many technologies hinge upon the performance of underlying materials. The efficiency of photovoltaic materials, for example, heavily depends on the electronic properties of the solid-state or organic semiconductors, or the stability of energy storage materials is governed by their energy landscapes and vibrational modes. With the help of modern compute hardware and *ab initio* theories, properties of materials can nowadays be predicted *in silico* before their assessment is carried out experimentally.^{1–7} Subsequent synthesis and characterization is costly and should focus only on those materials predicted to exhibit the most promising properties. Computational materials design procedures therefore hold much promise to lift some of the chemical challenges the world is facing today.

Finding materials with superior properties in chemi-

cal compound space (CCS), the space consisting of all possible materials,^{8,9} can be seen as a numerical optimization problem. Due to the immense amount of possible compounds and atomic configurations in CCS naive screening is prohibitive. The combinatorial nature of CCS implies that fast yet accurate property estimates, as well as efficient algorithms for searching, are desirable.^{10–13} Alchemical derivatives provide useful, chemically local, gradient information, suggesting the applicability of gradient-based algorithms to the design new materials. Alchemical derivatives were already employed to model the stability of binary solid mixtures within virtual crystal approximations^{14,15}. They have also afforded accurate predictions of various properties and compound classes within less approximate perturbation theory^{16–23}. For molecules and ionic crystals, even chemical accuracy can be achieved in terms of alchemical first order based estimates of relative energies when fixing number of valence electrons and geometry.^{24,25} Such constraints can also be met by several material classes of great interest, such as III-V semiconductors. Here, we rely on a materials design algorithm which combines alchemical gradients with stochastic sampling and which holds promise for general computational materials design campaigns. Using this algorithm, we have optimized III-V crystal mixtures consisting of $\text{Al}_x\text{Ga}_{1-x}\text{As}$ with respect to band structure, arguably one of the most important properties of semiconductors due to their many electronic applications.^{26–29} The algorithm is illustrated in Fig. 1.

Alchemical gradients are obtained as first order perturbation of the ground state energies and resulting from a linear interpolation between reference (ref) Hamiltonian, \hat{H}^{ref} , and target (tar) Hamiltonian, \hat{H}^{tar} ,

$$E^{\text{tar}} \approx E^{\text{pred}} = \langle \Psi^{\text{ref}} | \hat{H}^{\text{tar}} | \Psi^{\text{ref}} \rangle \quad (1)$$

where $|\Psi^{\text{ref}}\rangle$ is the wavefunction of the reference system.^{9,18,24} To estimate changes in band structure, the same formula is applied to each eigenvalue of \hat{H}^{tar} at any given wavevector \mathbf{k} using the corresponding eigenfunction $|\phi_{\mathbf{k}}^{\text{ref}}\rangle$. In Fig. S2, the predictive performance for band structures is illustrated using GaAs (AlAs) as a reference in order to predict AlAs (GaAs): Note how most of the details in the band structure are faith-

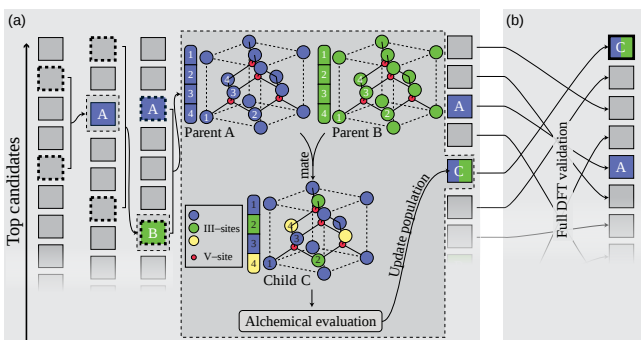


FIG. 1: Illustration of hybrid alchemical perturbation based genetic optimization used for $\text{Al}_x\text{Ga}_{1-x}\text{As}$ in 3x3x3 and 4x4x4 supercells. (a) Given 20 top crystal candidates (parents) with largest direct band gap, children are iteratively bred until they outperform at least one of the 20 top parents. The inset exemplifies the mating of randomly picked parent A and B which produce a top-performing child C in the third generation. C subsequently enters the updated pool of parents. This process is repeated until convergence, based on rankings exclusively obtained through alchemical perturbation estimates. Initialization corresponds to a single unperturbed self-consistent DFT calculation and 20 random perturbations. (b) Self-consistent DFT validation is carried out for all converged parents, leading to a slightly altered ranking.

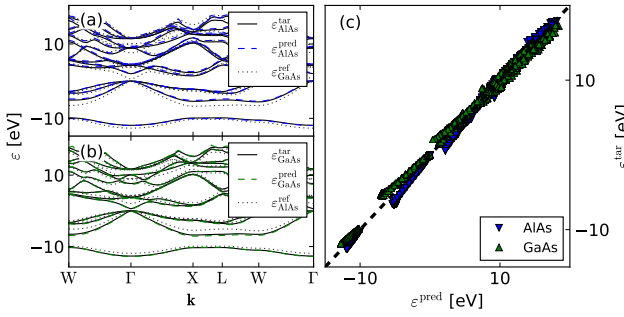


FIG. 2: AlAs Band structures (solid) predicted from alchemical predictions (dashed) using GaAs (dotted) as reference (a). GaAs Band structures (solid) predicted from alchemical predictions (dashed) using AlAs (dotted) as reference (b). Fermi level shifted to zero. (c) Scatter plot of alchemical prediction on every \mathbf{k} -point for all unoccupied and occupied bands. The mean absolute error for the latter amounts to 0.11 eV.

fully reproduced, and how the estimates can even account for the change from direct band gap with conduction band minimum at Γ for GaAs to indirect band gap with minimum at X for AlAs. The prediction error $\Delta\varepsilon_{\text{LUMO}}(\Gamma) = \varepsilon^{\text{pred}}(\Gamma) - \varepsilon^{\text{tar}}_{\text{LUMO}}(\Gamma)$ amounts to 0.25 (-0.2) eV, and $\Delta\varepsilon_{\text{LUMO}}(\text{X}) = 0.14$ (-0.15) eV for AlAs (GaAs) using GaAs (AlAs) as a reference. This implies a low band gap prediction error of only $\Delta E_g = 0.14$ eV and $\Delta E_g = -0.2$ eV for AlAs and GaAs, respectively. A scatter plot for estimates corresponding to every \mathbf{k} -point and every band is shown in Fig. S2(c), indicating a very good correlation. The mean absolute error (MAE) made when predicting eigenvalues for all occupied bands and \mathbf{k} -points is as low as 0.11 eV.

Numerical results with such predictive power suggest that first order alchemical estimates are sufficiently accurate for robust yet efficient optimizations of $\text{Al}_x\text{Ga}_{1-x}\text{As}$ based band structures. Unfortunately, due to the large dimensionality of the problem, it is still challenging to optimize the band structure using reliable gradients alone. For example, modeling a 3x3x3 supercell of pure GaAs, corresponding to 27 Ga atoms, implies a total compositional space of $2^{27} \sim 134$ million possible $\text{Al}_x\text{Ga}_{1-x}\text{As}$ combinations (not accounting for symmetry). Therefore, we have used the genetic optimization algorithm, described in Fig. 1 and based on alchemical perturbations towards the pseudopotential of Al at all Ga sites. Starting with a single unperturbed reference PBE DFT calculation, the corresponding direct band gap maximization history, on display in Fig. 3, indicates rapid convergence towards predicted PBE band gaps of ~ 1.6 eV after less than 800 generations. The optimization history for each generation (Fig. 3(a)) clearly illustrates how the average trend of direct E_g^{pred} is moving upward as the gradient sampling iterations proceed. These results imply that the mating procedure during hybrid optimization (Fig. 1(a)) systematically steers the population towards larger direct E_g . Since the band structure is determined

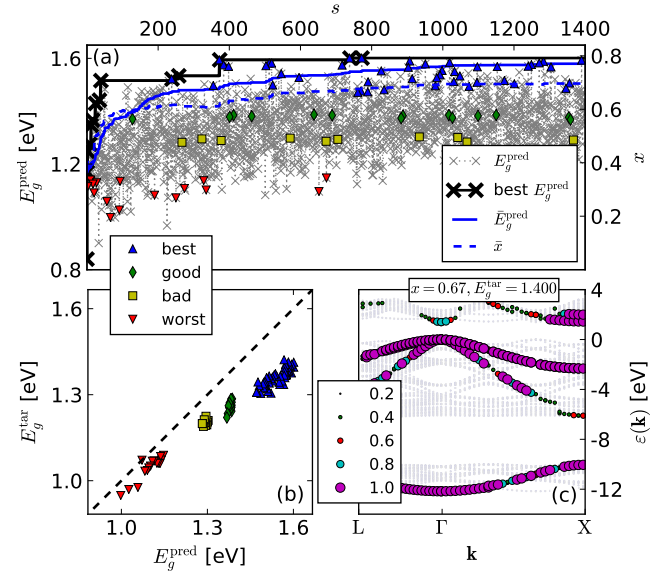


FIG. 3: (a) Band gap maximization history of genetic algorithm (see Fig. 1) based on alchemical perturbations to pure 3x3x3 GaAs super-cell. Predicted values, current best, average of top 20 crystals, and average mole fraction are indicated as gray crosses, black crosses, solid blue line, and dashed blue line, respectively. Randomly selected crystals with predicted worst, bad, good, and best band-gap are respectively denoted by lower triangle, square, diamond, and circle. (b) Scatter plot of E_g^{tar} vs. E_g^{pred} for best, good, bad, and worst crystals indicates that the overestimation of predicted band gap increases with true band gap. (c) Unfolded target band structure (circle size indicates weight) of converged $\text{Al}_{0.67}\text{Ga}_{0.33}\text{As}$ crystal with largest direct gap, the corresponding HSE calculation yields $E_g^{\text{HSE}} = 2.1$ eV.

by the structure of occupied and unoccupied orbitals, this also indicates that crystal truncation and catenation roughly preserve the local structure of orbitals around each atom. As a result, the algorithm identifies crystals with E_g^{pred} of around 1.6 eV after only several hundred iterations. Among the best ten crystals out of 1444 identified (table I) within hybrid optimization, a crystal $\text{Al}_{0.67}\text{Ga}_{0.33}\text{As}$ (structure shown in Fig. 4), with direct $E_g^{\text{tar}} = 1.4$ eV has been selected, and its unfolded^{30,31} target band structure is plotted in Fig. 3(c), where the spectral weight at Γ is 70.7%, and the band gap prediction error $|\Delta E_g| = 0.18$ eV. We also note that the average value of the top 20 candidates converges quickly within ~ 1000 generations.

For the select examples (best, good, bad, worst) a decent correlation between E_g^{pred} and E_g^{tar} is shown in Fig. 3(b) with a linear fit yielding MAE = 0.014 eV. Since the trends are preserved between E_g^{tar} and E_g^{pred} , one genetic optimization is sufficient to identify the global optima. Optimization performance obtained for other starting structures or larger super cells (see supplementary results) corroborates this observation, indicating significant robustness and generality of the design ap-

TABLE I: Direct band-gaps of the ten best alchemically optimized $\text{Al}_x\text{Ga}_{1-x}\text{As}$ crystal candidates, at HSE (E_g^{HSE}), PBE (E_g^{tar}), and alchemically (E_g^{pred}) calculated (using the PBE band structure of pure GaAs as reference) level of theory. Entries are ordered by E_g^{HSE} , ranking for PBE (tar) and alchemical (pred) estimates are given, as well as mole fraction x , and spectral weight at bottom of conduction band at Γ -point (w_{Γ}).

E_g^{HSE} [eV]	#(tar)	E_g^{tar} [eV]	#(pred)	E_g^{pred} [eV]	x	w_{Γ} (%)
2.100	1	1.400	8	1.583	0.67	70.72
2.099	10	1.414	9	1.583	0.74	61.39
2.098	2	1.406	3	1.594	0.74	62.34
2.098	9	1.413	2	1.601	0.74	59.77
2.098	6	1.400	6	1.589	0.74	59.43
2.098	7	1.390	10	1.582	0.67	67.89
2.096	4	1.396	1	1.601	0.70	65.48
2.096	3	1.376	4	1.593	0.67	67.63
2.096	8	1.397	5	1.590	0.70	63.40
2.095	5	1.382	7	1.585	0.70	63.47

proach. Consecutive optimizations confirm that the best crystals identified during each hybrid optimization are structurally similar (see Fig. 4(b)). HSE band gaps are known to be in better agreement with experiments than PBE.^{32,33} We have therefore calculated the corresponding HSE band gaps³⁴ for the ten best converged candidates, E_g^{HSE} , listed in Tab. I (coordinates are included in the supplementary materials). Due to HSE being computationally more demanding, we used the PBE weights for unfolding, assuming that they will negligibly affect the HSE gap. Throughout the optimization history, E_g^{pred} values cover a range of 0.9 eV to 1.6 eV, as plotted as a sorted sequence in Fig. 4(a). For mole fractions exceeding $x \approx 0.7$ the direct gap becomes indirect, in line with previous calculations.^{35–37}

To better understand what and how structural features impact changes in direct band gap, we have analyzed the crystal structures visited throughout the optimization history. We compare crystals with large and small band-gap using a periodic variant of the Coulomb matrix representation \mathbf{C} ^{38,39}, where

$$C_{IJ} = \begin{cases} 0 & \text{for } I = J \\ \frac{Z_I Z_J}{\min(\mathbf{R}_{IJ})} & \text{else} \end{cases} \quad (2)$$

with nuclear charges Z and minimal distances $\min(\mathbf{R}_{IJ})$ between periodic images of atom positions \mathbf{R}_I and \mathbf{R}_J . \mathbf{C} represents any crystal in a unique fashion and allows us to quantify the similarity between crystal \mathbf{C}_A and \mathbf{C}_B by the normalized matrix norm $\|\mathbf{C}_A - \mathbf{C}_B\| / \|\mathbf{C}_A\|$. Ranking as well as distributions of similarities to the top crystal (shown as inset) with the widest alchemically predicted direct band gap are presented in Fig. 4 for all crystals falling into the 2-200 (blue), 500-700 (green), and 1000-1200 (red) windows of candidate rank. Overall, and not surprisingly, the top crystals clearly indicate higher probability of being more similar to the top crystal (blue bars

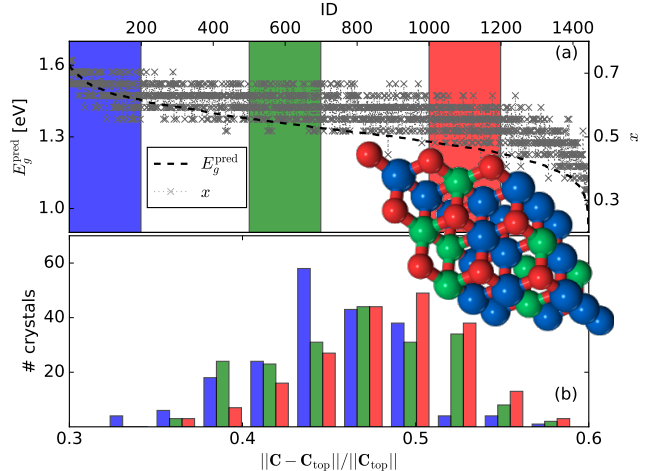


FIG. 4: (a) Sorted alchemically predicted E_g^{pred} from optimization history in descending order (black dashed), superimposed with mole fraction x in same order (dotted gray). (b) Normalized coulomb matrix based distance distribution between best crystal (shown as inset with Al, Ga, As in blue, green, and red, respectively) and crystals from three colored bands highlighted in (a) (200 crystals from each band).

larger than green and red for smaller similarity values. The histogram even suggests that for small similarity values smaller than 0.45, the periodic Coulomb matrix alone can be used as a descriptor to identify large direct band gap crystals with high probability. Encouragingly, the relative mutual similarity distributions for intermediate (green) and distant (red) crystal ranks are also consistent with the corresponding trends in band-gaps.

While large band-gap semi-conductors are of widespread interest, one might wonder if the alchemical approach is also applicable to other materials design problem. In order to explore the general applicability of alchemical derivatives for ranking crystals, we now also consider the alchemically predicted ranking among Ca and Sr alanates with respect to their potential for H_2 uptake. $\text{Ca}(\text{AlH}_4)_2$ and $\text{Sr}(\text{AlH}_4)_2$ release hydrogen when heated, and have been proposed as reversible hydrogen storage materials.^{40,41} We have investigated 42 Ca- and 44 Sr-alanate crystal polymorph structures from Ref. 42. We comply with the aforementioned constraint of fixed structure by generating all Sr-alanate (Ca-alanate) crystals with identical crystal structures for each Ca-alanate (Sr-alanate) crystal. The H_2 absorption energy of a Ca-alanate \hat{H}^{tar} is alchemically estimated using the Sr-alanate \hat{H}^{ref} in the same crystal lattice. Results in Fig. 5 indicate that the alchemical estimates correctly predict the energetically strongest Ca-alanate, and the three strongest Sr-alanates. Decent predictive power regarding the H_2 absorption energy ordering is also illustrated in Fig. 5(c) and (d) for the 60 most stable alanate crystals with a linear fit corresponding to a MAE of only 0.02 eV. The ranking error distribution (Fig. 5(d) inset) and a Spearman's rank correlation

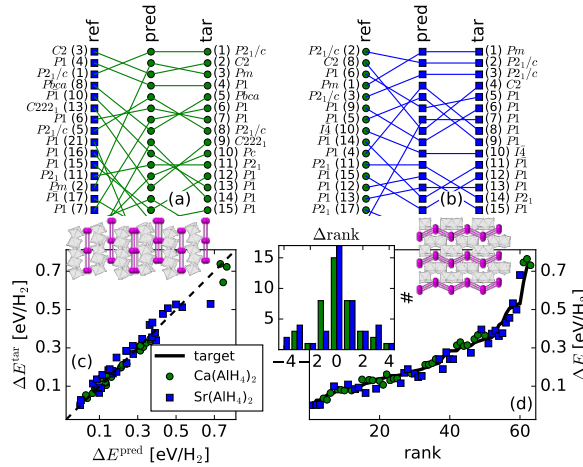


FIG. 5: H₂ absorption energy ranking of (a) Ca-alanates (tar) predicted by first order alchemical derivatives (pred) using Sr-alanates as reference systems (ref), and of (b) Sr-alanates (tar) predicted by first order alchemical derivatives (pred) using Ca-alanates as reference systems (ref). Crystal space groups and solid lines track individual crystals. Crystal structures of best Sr and Ca alanates are shown as an inset. (c) True absorption energy vs. alchemically predicted absorption energy of Ca(Sr)-alanates in green (blue) up to 0.8 eV/H₂ (relative to the best crystal), and (d) corresponding ranking of H₂ absorption energies by target (black line) and alchemically predicted (green and blue for predicting Ca and Sr-alanates, respectively). Error distributions in predicted ranking (Δrank) are shown as inset.

coefficient of 0.96 also indicate substantial predictive power, sufficient for most materials design purposes.

To conclude and summarize, we have presented numerical evidence for the usefulness of alchemical first order derivatives to tackle outstanding challenges in the realm of computational materials design, such as estimating H₂ absorption energy ordering across Ca and Sr-alanates of varying crystal structure. The focus of this study, however, has been to optimize band structures in III-V semiconductors, namely to maximize the direct band gap in Al_xGa_{1-x}As systems. Thanks to the computational efficiency of a gradient based genetic optimi-

mization algorithm, multiple Al_xGa_{1-x}As crystals with direct $E_g \approx 2.1$ eV and mole fraction $x \approx 0.7$ have been identified. The qualitative identification of crystals with the largest E_g within single optimization runs implies that the E_g surface is fairly flat in the crystal space of Al_xGa_{1-x}As systems. Future work will deal with extensions to higher orders.

Computational details Alchemical derivative and PBE results are computed using the ABINIT package⁴³ with Goedecker norm-conserving pseudopotentials^{44,45} and planewave cutoff of 100 Ry. Monkhorst-Pack⁴⁶ $6 \times 6 \times 6$ mesh for fcc primitive cell band structure, and $3 \times 3 \times 3$ mesh for band structure optimization (both for $3 \times 3 \times 3$ and $4 \times 4 \times 4$ fcc supercell) are used respectively. VASP⁴⁷ package with PAW⁴⁸ pseudopotentials with default cutoff are used for HSE⁴⁹ results for Al_xGa_{1-x}As $3 \times 3 \times 3$ fcc supercell. 10 and 16 virtual orbitals are used for fcc primitive and supercells respectively. Experimental lattice constants (if available) are used for every crystal considered in this report. Otherwise calculated values are used from the literature (see table SI in supplemental materials). Alchemical derivatives are printed by restarting with the reference wavefunction in ABINIT, and setting the SCF iteration step to 0 to evaluate $\partial_\lambda E$. Three independent optimizations have been carried out for $3 \times 3 \times 3$ fcc supercells, and one optimization for a $4 \times 4 \times 4$ fcc supercell. Gradient sampling is carried out with population size of 20 and mutation rate of 0.5%. Pseudocode and convergence criteria have been included in the supplementary material. The $3 \times 3 \times 3$ fcc supercell crystal is extended to $9 \times 9 \times 9$ fcc supercell to compute the periodic Coulomb matrix in order to account for all possible periodic images.

I. ACKNOWLEDGEMENTS

OAvL acknowledges support by the Swiss National Science foundation (No. PP00P2_138932, 407540_167186 NFP 75 Big Data, 200021_175747, NCCR MARVEL). Some calculations were performed at sciCORE (<http://scicore.unibas.ch/>) scientific computing core facility at University of Basel.

* Electronic address: anatole.vonlilienfeld@unibas.ch

¹ F. Capasso, “Band-gap engineering: From physics and materials to new semiconductor devices,” *Science*, vol. 235, p. 172, 1987.

² S. R. Marder, D. N. Beratan, and L. T. Ceng, “Approaches for optimizing the first electronic hyperpolarizability of conjugated organic molecules,” *Science*, vol. 252, p. 103, 1991.

³ G. H. Jóhannesson, T. Bligaard, A. V. Ruban, H. L. Skriver, K. W. Jacobsen, and J. K. Nørskov, “Combined electronic structure and evolutionary search approach to materials design,” *Phys. Rev. Lett.*, vol. 88, p. 255506,

2002.

⁴ W. L. Jorgensen, “The many roles of computation in drug discovery,” *Science*, vol. 303, p. 1813, 2004.

⁵ C. Oostenbrink and W. F. van Gunsteren, “Free energies of ligand binding for structurally diverse compounds,” *Proc. Natl. Acad. Sci. USA*, vol. 102, p. 6750, 2005.

⁶ T. F. T. Cerqueira, R. Sarmiento-Pérez, M. Amsler, F. Nogueira, S. Botti, and M. A. L. Marques, “Materials design on-the-fly,” *J. Chem. Theory Comput.*, vol. 11, p. 3955, 2015.

⁷ M. C. Toroker and E. A. Carter, “Transition metal oxide alloys as potential solar energy conversion materials,” *J.*

Mater. Chem. A, vol. 1, p. 2474, 2013.

⁸ P. Kirkpatrick and C. Ellis, "Chemical space," *Nature*, vol. 432, p. 823, 2004.

⁹ O. A. von Lilienfeld, "First principles view on chemical compound space: Gaining rigorous atomistic control of molecular properties," *Int. J. Quantum Chem.*, vol. 113, p. 1676, 2013.

¹⁰ A. Franceschetti and A. Zunger, "The inverse band-structure problem of finding an atomic configuration with given electronic properties," *Nature*, vol. 402, p. 60, 1999.

¹¹ M. Wang, X. Hu, D. N. Beratan, and W. Yang, "Designing molecules by optimizing potentials," *J. Am. Chem. Soc.*, vol. 128, p. 3228, 2006.

¹² T. Weymuth and M. Reiher, "Inverse quantum chemistry: Concepts and strategies for rational compound design," *Int. J. Quantum Chem.*, vol. 114, p. 823, 2014.

¹³ F. D. Vleeschouwer, P. Geerlings, and F. D. Proft, "Molecular property optimization with boundary conditions through the best first search scheme," *Comput. Phys. Comm.*, vol. 17, p. 1391, 2016.

¹⁴ N. Marzari, S. de Gironcoli, and S. Baroni, "Structure and phase stability of $\text{Ga}_x\text{In}_{1-x}\text{P}$ solid solutions from computational alchemy," *Phys. Rev. Lett.*, vol. 72, p. 4001, 1994.

¹⁵ M. d'Avezac and A. Zunger, "Identifying the minimum-energy atomic configuration on a lattice: Lamarckian twist on Darwinian evolution," *Phys. Rev. B*, vol. 78, p. 064102, 2008.

¹⁶ O. A. von Lilienfeld, R. D. Lins, and U. Rothlisberger, "Variational particle number approach for rational compound design," *Phys. Rev. Lett.*, vol. 95, p. 153002, 2005.

¹⁷ O. A. von Lilienfeld and M. E. Tuckerman, "Molecular grand-canonical ensemble density functional theory and exploration of chemical space," *J. Chem. Phys.*, vol. 125, p. 154104, 2006.

¹⁸ O. A. von Lilienfeld, "Accurate *ab initio* energy gradients in chemical compound space," *J. Chem. Phys.*, vol. 131, p. 164102, 2009.

¹⁹ R. Balawender, M. A. Welearegay, M. Lesiuk, F. De Proft, and P. Geerlings, "Exploring chemical space with the alchemical derivatives," *J. Chem. Theory Comput.*, vol. 9, p. 5327, 2013.

²⁰ P. Geerlings, S. Fias, Z. Boisdenghen, and F. De Proft, "Conceptual DFT: Chemistry from the linear response function," *Chem. Soc. Rev.*, vol. 43, p. 4989, 2014.

²¹ Y. S. Al-Hamdani, A. Michaelides, and O. A. von Lilienfeld, "Exploring dissociative water adsorption on isoelectronically BN doped graphene using alchemical derivatives," *J. Chem. Phys.*, vol. 147, p. 164113, 2017.

²² R. A. M.- Quintana and P. W. Ayers, "Interpolating hamiltonians in chemical compound space," *Int. J. Quantum Chem.*, vol. 117, p. 25384, 2017.

²³ K. Saravanan, J. R. Kitchin, O. A. von Lilienfeld, and J. A. Keith, "Alchemical predictions for computational catalysis: Potential and limitations," *J. Phys. Chem. Lett.*, vol. 8, p. 5002, 2017.

²⁴ K. Y. S. Chang, S. Fias, R. Ramakrishnan, and O. A. von Lilienfeld, "Fast and accurate predictions of covalent bond in chemical space," *J. Chem. Phys.*, vol. 144, p. 174100, 2016.

²⁵ A. Solovyeva and O. A. von Lilienfeld, "Alchemical screening of ionic crystals," *Phys. Chem. Chem. Phys.*, vol. 18, p. 31078, 2016.

²⁶ D. L. Smith and C. Mailhiot, "Theory of semiconductor superlattice electronic structure," *Rev. Mod. Phys.*, vol. 62, p. 173, 1990.

²⁷ O. A. von Lilienfeld and P. A. Schultz, "Structure and band gaps of Ga-(V) semiconductors: The challenge of Ga pseudopotentials," *Phys. Rev. B*, vol. 77, p. 115202, 2008.

²⁸ J. Liqiang, Q. Yichun, W. Baiqi, L. Shudan, J. Baojiang, Y. Libin, F. Wei, F. Hunggang, and S. Jiazhong, "Review of photoluminescence performance of nano-sized semiconductor materials and its relationships with photocatalytic activity," *Sol. Energ. Mat. Sol. Cells*, vol. 90, p. 1773, 2006.

²⁹ N. López, L. A. Reichertz, K. M. Yu, and W. Walukiewicz, "Engineering the electronic band structure for multiband solar cells," *Phys. Rev. Lett.*, vol. 106, p. 028701, 2011.

³⁰ O. Rubel, A. Bokhanchuk, S. J. Ahmed, and E. Assmann, "Unfolding the band structure of disordered solids: From bound states to high-mobility Kane-fermions," *Phys. Rev. B*, vol. 90, p. 115202, 2014.

³¹ V. Popescu and A. Zunger, "Effective band structure of random alloys," *Phys. Rev. Lett.*, vol. 104, p. 236403, 2010.

³² J. Heyd and G. E. Scuseria, "Efficient hybrid density functional calculations in solids: Assessment of the Heyd-Scuseria-Ernzerhof screened Coulomb hybrid functional," *J. Chem. Phys.*, vol. 121, p. 1187, 2004.

³³ J. Heyd, J. E. Peralta, G. E. Scuseria, and R. L. Martin, "Energy band gaps and lattice parameters evaluated with the Heyd-Scuseria-Ernzerhof screened hybrid functional," *J. Chem. Phys.*, vol. 123, p. 174101, 2005.

³⁴ E. R. Batista, J. Heyd, R. G. Hennig, B. P. Uberuaga, R. L. Martin, and G. E. Scuseria, "Comparison of screened hybrid density functional theory to diffusion Monte Carlo in calculations of total energies of silicon phases and defects," *Phys. Rev. B*, vol. 74, p. 131102, 2006.

³⁵ L. Bellaiche and D. Vanderbilt, "Virtual crystal approximation revisited: Application to dielectric and piezoelectric properties of perovskites," *Phys. Rev. B*, vol. 61, p. 7877, 2000.

³⁶ J. W. Nicklas and J. W. Wilkins, "Accurate *ab initio* prediction of III-V direct-indirect band gap crossovers," *Appl. Phys. Lett.*, vol. 97, p. 091902, 2010.

³⁷ S. H. Wei, L. G. Ferreira, J. E. Bernard, and A. Zunger, "Electronic properties of random alloys: Special quasirandom structures," *Phys. Rev. B*, vol. 42, p. 9622, 1990.

³⁸ M. Rupp, A. Tkatchenko, K. R. Müller, and O. A. von Lilienfeld, "Fast and accurate modeling of molecular atomization energies with machine learning," *Phys. Rev. Lett.*, vol. 108, p. 058301, 2012.

³⁹ F. Faber, A. Lindmaa, O. A. von Lilienfeld, and R. Armiento, "Crystal structure representations for machine learning models of formation energies," *Int. J. Quantum Chem.*, vol. 115, p. 1094, 2015. <http://arxiv.org/abs/1503.07406>.

⁴⁰ L. Schlapbach and A. Züttel, "Hydrogen-storage materials for mobile applications," *Nature*, vol. 414, p. 353, 2001.

⁴¹ T. K. Mandal and D. H. Gregory, "Hydrogen storage materials: Present scenarios and future directions," *Annu. Rep. Prog. Chem., Sect. A*, vol. 105, p. 21, 2009.

⁴² T. D. Huan, M. Amsler, M. A. L. Marques, S. Botti, A. Willand, and S. Goedecker, "Low-energy polymeric phases of alanates," *Phys. Rev. Lett.*, vol. 110, p. 135502, 2013.

⁴³ X. Gonze, B. Amadon, P. M. Anglade, and J. M. Beuken, "ABINIT: First-principle approach to material and nanosystem properties," *Comput. Phys. Comm.*, vol. 180, p. 2582, 2002.

⁴⁴ M. Krack, "Pseudopotentials for H to Kr optimized

for gradient-corrected exchange-correlation functionals,” *Theor. Chim. Acta*, vol. 114, p. 145, 2005.

⁴⁵ C. Hartwigsen, S. Goedecker, and J. Hutter, “Relativistic separable dual-space Gaussian pseudopotentials from H to Rn,” *Phys. Rev. B*, vol. 58, p. 3641, 1998.

⁴⁶ H. J. Monkhorst and J. D. Pack, “Special points for Brillouin-zone integrations,” *Phys. Rev. B*, vol. 13, p. 5188, 1976.

⁴⁷ G. Kresse and J. Furthmüller, “Efficient iterative schemes for ab initio total-energy calculations using a plane-wave basis set,” *Phys. Rev. B*, vol. 54, p. 11169, 1996.

⁴⁸ G. Kresse and D. Joubert, “From ultrasoft pseudopotentials to the projector augmented-wave method,” *Phys. Rev. B*, vol. 59, p. 1758, 1999.

⁴⁹ A. V. Krukau, O. A. Vydrov, A. F. Izmaylov, and G. E. Scuseria, “Influence of the exchange screening parameter on the performance of screened hybrid functionals,” *J. Chem. Phys.*, vol. 125, p. 224106, 2006.

Supplemental Materials

II. III-V AND IV-IV SEMICONDUCTORS

Alchemical prediction from the reference material of lattice constant a to any target material (tar) on the i^{th} band at a given crystal momentum \mathbf{k} is constructed as follows: $\varepsilon_{i,a}^{\text{pred}}(\mathbf{k}) = \varepsilon_{i,a}^{\text{ref}}(\mathbf{k}) + \partial_\lambda \varepsilon_{i,a}^{\text{ref} \rightarrow \text{tar}}(\mathbf{k})$, where the derivative is a 3D integral, $\partial_\lambda \varepsilon_{i,a}^{\text{ref} \rightarrow \text{tar}}(\mathbf{k}) = \langle \phi_{i\mathbf{k}}^{\text{ref}} | H_{\text{tar}} - H_{\text{ref}} | \phi_{i\mathbf{k}}^{\text{ref}} \rangle_a$, calculated from the i^{th} orbital of the reference material of lattice constant a with crystal momentum \mathbf{k} . The prediction of band gap is defined as:

$$E_{g,a}^{\text{pred}} = \min_{\mathbf{k}} (\varepsilon_{\text{LUMO},a}^{\text{pred}}(\mathbf{k}) - \varepsilon_{\text{HOMO},a}^{\text{pred}}(\mathbf{k})), \quad (\text{S1})$$

where the maximum of conduction band of materials investigated is located at Γ -point. A predicted band gap is direct if the predicted minimum of $\varepsilon_{\text{LUMO}}$ is located at Γ -point. Lattice constants for the semiconductors are scanned from 5.4 Å to 6.5 Å in step of 0.05 Å including extra points correspond to the lattice constant reported in the literature. This range covers all equilibrium constants reported for all the semiconductors considered.

We quantify the performance of our predictions using the mean absolute error (MAE) of a prediction to the entire i^{th} band of a target material at lattice constant a , made from some reference material as

$$\text{MAE}_{i,a}(\text{ref, tar}) = \sum_{\mathbf{k}} |\varepsilon_{i,a}^{\text{pred}}(\mathbf{k}) - \varepsilon_{i,a}^{\text{true}}(\mathbf{k})| w(\mathbf{k}), \quad (\text{S2})$$

where $\varepsilon_{i,a}(\mathbf{k})$ is the i^{th} eigenvalue of Hamiltonian at lattice constant a and crystal momentum \mathbf{k} . $w(\mathbf{k})$ is the corresponding Monkhorst-Pack⁴⁶ weight for the sampled special \mathbf{k} -points. Throughout this paper, the error reported corresponds to average over all bands and lattice constants. The subscripts i and a are omitted unless noted otherwise.

The averaged MAE over all lattice constants and bands for all combinations of reference/target pair, or alchemical path, is on display in the upper panels in Fig. S1. Overall, decent agreements are found with most predictions being in agreement with the target by less than 0.5 eV. Alchemical estimates with averaged MAE less than 0.2 eV are highlighted by the white circles. A general trend can be observed: Predictions using semiconductors containing 3rd-row elements in the reference give overall the largest averaged MAE, when the target material has elements from the 5th row, as can be seen by the red/orange corner of the upper panels (left for III-V semiconductors and right for IV-IV semiconductors) in Fig. S1. A similar target-reference pattern has been observed for alchemical predictions of covalent bonding, and is due to lack of similarity of electron densities.^{24,25}

A scatter plot between averaged MAE and integrated absolute electron density difference, defined as $|\Delta\rho(\mathbf{r})| = |\rho_{\text{tar}}(\mathbf{r}) - \rho_{\text{ref}}(\mathbf{r})|$, is shown in the lower left panel in Fig. S1. The results suggest that there is an upper error bound: Any alchemical path with small density changes will give a small predictive error to band structure, as all the points lie beneath the red dotted line. However, a small error does not necessarily imply small density changes, as many results with small predictive error correspond to large density changes. This is because the band structure is determined by the relative differences in Hamiltonian eigenvalues and the corresponding orbital structure. Cancellation of higher order (curvature) effects along the alchemical path can lead to a small predictive error for first order estimates yet large density change. Similar error cancellation has also been discussed in the context of covalent bonding Ref. 24. The fact that small density changes imply accurate predictions can be used as a sufficient condition to detect good predictive power. This might be useful for future studies if decent approximations to inexpensively estimate electron density changes can be found. The region with $\int d\mathbf{r} |\Delta\rho(\mathbf{r})| < 0.5$ a.u. electron/primitive cell is highlighted by the white background in the lower left panel. The band gap predictions of the corresponding alchemical paths highlighted as white crosses in the upper panels of Fig. S1. A scatter plot versus the true band gap is shown in the lower right panel, remarkable agreement is found with MAE of less than 0.05 eV. The linear fit gives $E_g^{\text{true}} \approx 0.93 E_g^{\text{pred}} + 0.019$ eV, with $R^2 = 0.93$, RMSE = 0.047 eV and MAE = 0.036 eV. The negative E_g in the lower right panel of Fig. S1 correspond to GaSb and InSb with small lattice constants. In such environment, the conduction band minimum is lower than the valence band maximum. Notice that decent predictive power can be achieved by alchemical predictions, satisfying the sufficient condition above, even at such extreme situation.

It is possible to use III-V semiconductor reference calculations to predict the band structure of other IV-IV semiconductors. However, such interpolations do not provide satisfactory predictive power when using only first order alchemical derivatives, due to the dissimilarity of the electronic density. Similar conclusions hold when attempting to predict band structures of II-VI semiconductors using III-V reference densities.

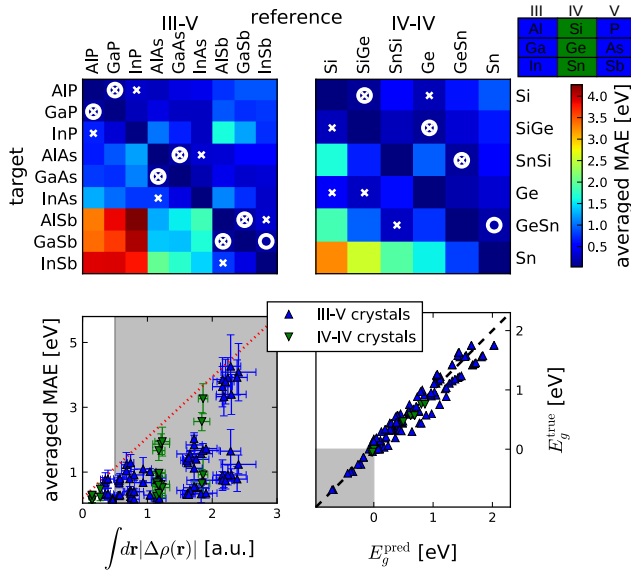


FIG. S1: Prediction errors of band structure on alchemical paths for III-V (upper left) and IV-IV (upper right) semiconductors. Errors less than 0.2 eV are highlighted by white circles. Combinations with $\int dr |\Delta\rho(\mathbf{r})| < 0.5$ a.u. are highlighted by white crosses. For guidance, the relevant block in the periodic table is shown in the top right corner. The lower left panel: Correlation of averaged MAE and integrated density difference for III-V and IV-IV semiconductors. The error bars represent the variations due to changes in lattice constant of the corresponding term. The lower right panel: Scatter plot of band gap prediction vs. true for alchemical paths with $\int dr |\Delta\rho(\mathbf{r})| < 0.5$ a.u..

TABLE SI: Lattice constants of III-V and IV-IV semiconductors in Å. Most of the lattice constants are taken from Ref. S1, while SnSi from Ref. S2, GeSn from Ref. S3, and SiGe from Ref. S4

AlP	5.4635	AlAs	5.6600	AlSb	6.1355	Si	5.4310	SiGe	5.4320
GaP	5.4510	GaAs	5.6535	GaSb	6.0900	Ge	5.6580	GeSn	6.0758
InP	5.8600	InAs	6.0500	InSb	6.4700	SnSi	5.9610	Sn	6.4892

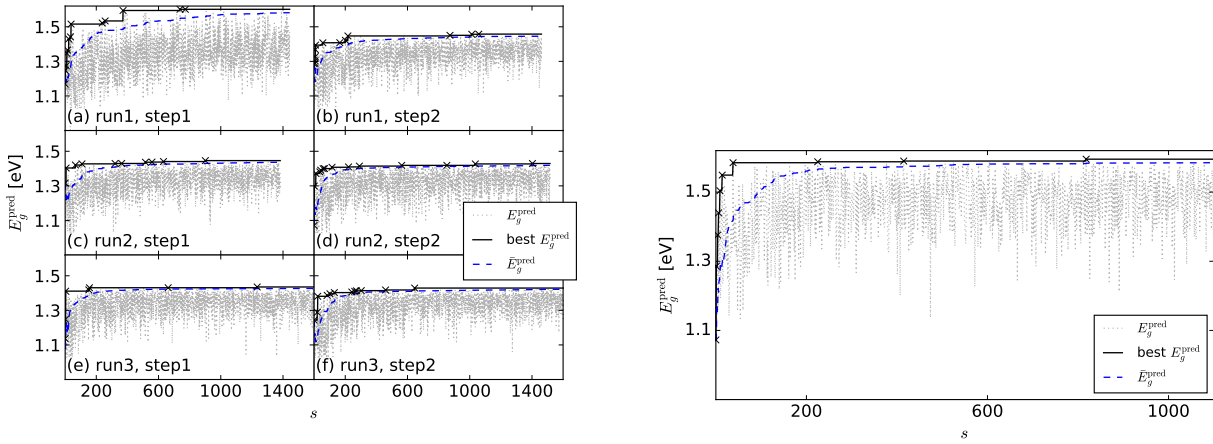


FIG. S2: LEFT: Three optimization runs with different initial distributions of atoms, once pristine GaAs (top), and twice Ga/Al distributed at random (left), and after restarting the optimization using the wave function of the converged system (right) in $3 \times 3 \times 3$ super cells. RIGHT: Optimization run starting with random initial atomic positions in $4 \times 4 \times 4$ super cell.

III. OPTIMIZATION

The objective of the gradient-based GA optimization is set to maximize the band gap while the bottom of the conduction band must be located at Γ -point in the Brillouin zone. To this end, we vary the mixing ratio of Al and Ga, as well as their location. Instead of performing a DFT evaluation for each candidate crystal, the band structure of a candidate crystal is estimated using alchemical derivatives. Each alchemical prediction takes less than 1% of the computational cost for a full DFT band structure calculation. This enables the rapid exploration of many configurations and mixture ratios with decent accuracy. The Brillouin zone of the supercell is unfolded and corresponds to the one from a primitive cell using spectral weights.^{30,31}

Three independent gradient-based GA optimizations have been carried out, start with three starting crystals: Pure GaAs and two random crystals, where either Ga or Al is randomly chosen for each of 27 III-sites. All three optimizations converged within two optimization steps, which give total six GA sampling histories. 3137 crystals have been evaluated in the first GA sampling history. Out of these, 1444 are predicted to be direct band gap crystal. Roughly half of the searched crystals are of indirect band gap. E_g^{true} are calculated for the following four groups of crystals from the first GA sampling step history, depending on the sorted direct band gap predictions: the best 50 E_g^{best} , the top 491 to 504 E_g^{good} , the top 1001 to 1010 E_g^{bad} , and the worst 15 E_g^{worst} . The analysis of the first GA sampling history is shown in Fig. 3, while the analysis of all three optimization histories is presented in Fig. 4. Pseudocode for the gradient-based optimization is presented in the pseudo-code below, where each of the routines corresponds to the following.

- **optimization:** The main routine consist of: A stochastic sampling procedure; and a gradient step that updates wavefunction by full DFT evaluation, as schematically shown in the left panel of Fig. 1. The convergence criterion $|E_g^h - E_g^{(h-1)}| < 0.001$ eV at h^{th} optimization step.
- **full DFT:** It performs full DFT evaluations on the requested crystals and returns the best corresponding true band gap, E_g^{true} , and orbitals, $\{\phi_i\}$.
- **GA sampling:** The routine stochastically samples the alchemical estimates, using reference orbitals $\{\phi_i\}$. The initial population of twenty crystals is randomly generated. The best five crystals are used for full DFT evaluation. The sampling criterion is at least 1400 crystals with direct band gap are found. And the difference between the average of the top-20 population, \bar{E}_g^{pred} , and the best-predicted crystal, E_g^{best} , is less than 0.02 eV.
- **get parents:** At each iteration during GA sampling, two parents, **ParentA** and **ParentB**, are randomly drawn from the top-20 of all searched crystals. In other words, the population size of GA is twenty.
- **mate:** The routine to generate a child from two parent crystals. The occupancy at each of the III-sites in the child crystal is randomly inherited from either parent with 50/50 possibility, as illustrated in the right panel of Fig. 1. A mutation rate of 0.05% is used at each of the III-sites, where the atom type would flip from Al to Ga or vise versa as indicated the yellow atom in the right panel of Fig. 1.
- **alchemical evaluation** estimate the band structure of the requested crystal using reference orbital $\{\phi_i\}$. If the prediction of the band gap is indirect, the value of the direct band gap is set to 0.

* Electronic address: anatole.vonlilienfeld@unibas.ch

[S1] M. Levinshtein, S. Rumyantsev, and M. Shur, *Handbook series on Semiconductor Parameters*. World Scientific, 1st ed., 1999.

[S2] A. Tonkikh, A. Klavsyuk, N. Zakharov, A. Saletsky, and P. Werner, “SnSi nanocrystals of zinc blende structure in a Si matrix,” *Nano Res.*, vol. 8, p. 3905, 2015.

[S3] N. Bhargava, M. Coppinger, J. P. Gupta, L. Wielunski, and J. Kolodzey, “Lattice constant and substitutional composition of GeSn alloy grown by molecular beam epitaxy,” *Appl. Phys. Lett.*, vol. 103, p. 041908, 2013.

[S4] M. M. Rieger and P. Vogl, “Electronic-band parameters in strained $\text{Si}_{1-x}\text{Ge}_x$ alloys on $\text{Si}_{1-y}\text{Ge}_y$ substrates,” *Phys. Rev. B*, vol. 48, p. 14276, 1993.

Algorithm S1 Gradient-based/genetic algorithm using alchemical derivative for crystal optimization. The pseudocode of the main routine, optimization, and two primary functions, full DFT and GA sampling, are explicitly stated. The variables are denoted by **typewriter** font.

```

procedure optimization(starting_crystal)
   $E_g^{(0)} \leftarrow 0$ 
   $h \leftarrow 1$ 
   $(E_g^{(h)}, \{\phi_i^{(h)}\}) \leftarrow \text{full DFT}(\text{starting_crystal})$ 
  while  $|E_g^{(h)} - E_g^{(h-1)}| > 0.001 \text{ eV}$  do
    top_5_predicted_crystals  $\leftarrow \text{GA sampling}(\{\phi_i^{(h)}\})$ 
     $(E_g^{(h+1)}, \{\phi_i^{(h+1)}\}) \leftarrow \text{full DFT}(\text{top_5_predicted_crystals})$ 
     $h \leftarrow h + 1$ 

function full DFT(crystals)
  preform full DFT evaluations on every crystals
  return  $(E_g^{\text{true}}, \{\phi_i\})$  of the best crystal among crystals

function GA sampling( $\{\phi_i\}$ )
  initialize population of size 20
   $E_g^{\text{pred}} \leftarrow \text{alchemical evaluation}(\{\phi_i\}, \text{population})$ 
   $s \leftarrow 1$ 
  while  $s < 1400$  and  $|\bar{E}_g^{\text{pred}} - E_g^{\text{best}}| < 0.02 \text{ eV}$  do
    (ParentA, ParentB)  $\leftarrow \text{get parent}(\text{population})$ 
    Child  $\leftarrow \text{mate}(\text{ParentA}, \text{ParentB})$ 
    if Child is not in population then
       $E_g^{\text{pred}} \leftarrow \text{alchemical evaluation}(\{\phi_i\}, \text{Child})$ 
      update population
    if  $E_g^{\text{pred}}$  is direct then
       $s \leftarrow s + 1$ 
  return top 5 crystals in the population

```

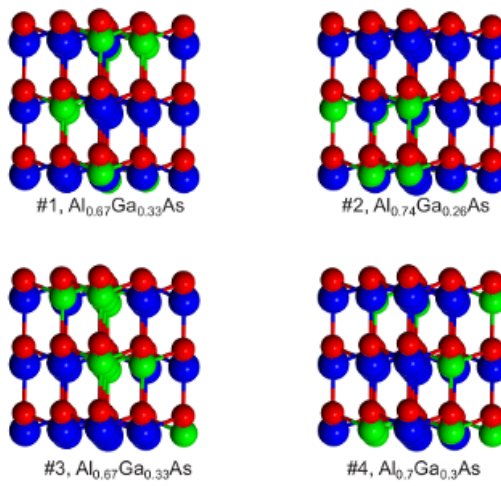


FIG. S3: The best four crystals with $E_g^{\text{HSE}} \approx 2.1 \text{ eV}$ according to Table. I. The HSE ordering rank and the crystal formula with mole fraction is shown for each crystal. The $3 \times 3 \times 3$ supercell is extended to $6 \times 6 \times 6$ to illustrate 2-fold symmetry, where Al, Ga, and As are represented by blue, green, and red spheres.

TABLE SII: $3 \times 3 \times 3$ super-cells for 10 top crystals with large direct band-gap (in the order of predicted gap in Table I in main text). Each column corresponds to a crystal, each row to the atomic site. Upper and lower block correspond to III and V elements, respectively

# \ rank	1	2	3	4	5	6	7	8	9	10	(x, y, z) [Å]
1	Al	Ga	Al	Ga	Ga	Al	Al	Ga	Al	Ga	(0.0, 0.0, 0.0)
2	Ga	Al	Ga	Al	Ga	Al	Al	Al	Ga	Al	(4.0, 0.0, 0.0)
3	Al	Al	Al	Ga	Al	Al	Al	Ga	Al	Al	(8.0, 0.0, 0.0)
4	Al	Al	Al	Ga	Al	Ga	Al	Al	Al	Al	(2.0, 3.5, 0.0)
5	Ga	Ga	Al	Ga	Al	Ga	Al	Ga	Ga	Ga	(6.0, 3.5, 0.0)
6	Al	Ga	Al	Al	Al	Al	Ga	Al	Al	Al	(10.0, 3.5, 0.0)
7	Al	(4.0, 6.9, 0.0)									
8	Al	Al	Ga	Al	Ga	Ga	Ga	Al	Ga	Ga	(8.0, 6.9, 0.0)
9	Al	Al	Al	Al	Al	Ga	Al	Al	Al	Ga	(12.0, 6.9, 0.0)
10	Al	Al	Al	Al	Al	Ga	Al	Ga	Ga	Al	(2.0, 1.2, 3.3)
11	Al	Al	Al	Al	Ga	Al	Al	Al	Al	Al	(6.0, 1.2, 3.3)
12	Al	Ga	Ga	Al	Al	Al	Ga	Ga	Al	Al	(10.0, 1.2, 3.3)
13	Ga	Al	Al	Ga	Al	Al	Ga	Al	Al	Ga	(4.0, 4.6, 3.3)
14	Al	Al	Al	Al	Ga	Al	Al	Al	Al	Al	(8.0, 4.6, 3.3)
15	Al	Al	Ga	Al	(12.0, 4.6, 3.3)						
16	Al	Al	Al	Al	Al	Al	Ga	Al	Ga	Ga	(6.0, 8.1, 3.3)
17	Ga	Al	Ga	Al	Al	Ga	Al	Ga	Al	Al	(10.0, 8.1, 3.3)
18	Al	Al	Al	Ga	Al	Al	Ga	Al	Al	Ga	(14.0, 8.1, 3.3)
19	Al	Al	Al	Ga	Al	Al	Al	Al	Al	Al	(4.0, 2.3, 6.5)
20	Ga	Ga	Al	Al	Al	Al	Ga	Al	Al	Ga	(8.0, 2.3, 6.5)
21	Al	Al	Ga	Al	(12.0, 2.3, 6.5)						
22	Al	(6.0, 5.8, 6.5)									
23	Al	Ga	Al	Ga	Al	Ga	Al	Al	Al	Ga	(10.0, 5.8, 6.5)
24	Ga	Ga	Al	Al	Al	Al	Ga	Al	Al	Al	(14.0, 5.8, 6.5)
25	Ga	Al	Al	Al	Ga	Al	Al	Ga	Ga	Al	(8.0, 9.2, 6.5)
26	Ga	Al	Al	Al	Ga	Al	Ga	Al	Ga	Al	(12.0, 9.2, 6.5)
27	Al	Al	Ga	Ga	Ga	Al	Al	Ga	Al	Al	(16.0, 9.2, 6.5)
28	As	(2.0, 1.2, 0.8)									
29	As	(6.0, 1.2, 0.8)									
30	As	(10.0, 1.2, 0.8)									
31	As	(4.0, 4.6, 0.8)									
32	As	(8.0, 4.6, 0.8)									
33	As	(12.0, 4.6, 0.8)									
34	As	(6.0, 8.1, 0.8)									
35	As	(10.0, 8.1, 0.8)									
36	As	(14.0, 8.1, 0.8)									
37	As	(4.0, 2.3, 4.1)									
38	As	(8.0, 2.3, 4.1)									
39	As	(12.0, 2.3, 4.1)									
40	As	(6.0, 5.8, 4.1)									
41	As	(10.0, 5.8, 4.1)									
42	As	(14.0, 5.8, 4.1)									
43	As	(8.0, 9.2, 4.1)									
44	As	(12.0, 9.2, 4.1)									
45	As	(16.0, 9.2, 4.1)									
46	As	(6.0, 3.5, 7.3)									
47	As	(10.0, 3.5, 7.3)									
48	As	(14.0, 3.5, 7.3)									
49	As	(8.0, 6.9, 7.3)									
50	As	(12.0, 6.9, 7.3)									
51	As	(16.0, 6.9, 7.3)									
52	As	(10.0, 10.4, 7.3)									
53	As	(14.0, 10.4, 7.3)									
54	As	(18.0, 10.4, 7.3)									